applied sciences

MDPI

Article

Enhancements of an Ocean Radar System for Improved Wind Observations in Weather Monitoring Operations

David Hui [1], Ching-Chi Lam [1], Pak-Wai Chan [1,*], Caijing Huang [2] and Shu Yang [3]

[1] Hong Kong Observatory, Hong Kong, China; cclam@hko.gov.hk (C.-C.L.)
[2] South China Sea Bureau, Ministry of Natural Resources, Guangzhou 510310, China; huangcaijing15@mails.ucas.ac.cn
[3] China Precise Ocean Detection Technology, Yichang 443000, China
* Correspondence: pwchan@hko.gov.hk

Abstract

In March 2021, a trial operation set of ocean radar was first introduced in Hong Kong, and then in early 2022 became stably paired up with one operated by the South China Sea Bureau of the Ministry of Natural Resources of China for filling up the meteorological data void over the eastern part of the South China coastal waters. The ocean radar has undergone various enhancements of hardware and software over the years and has reached a stage of providing useful wind observations for weather monitoring purposes in the majority of cases. This paper documents the novel features of the hardware and software of the ocean radar. The performance of the derived wind and other data from the ocean radar is studied by comparing with two sets of weather buoy observations over an extended period of time (one year from June 2024 to July 2025). The quality of the wind data is considered to be reasonable as compared with the international standards of wind measurement errors. The application of the ocean radar wind observations in monitoring different weather systems is also described, including monsoon surges, surface troughs of low pressure, rainstorms and tropical cyclones. The radar is still found to have difficulties in retrieving the winds of high strength (hurricane force winds) and the circulating flow at the same time. Further research work with the ocean radar is also discussed.

Keywords: ocean radar; wind observations; weather monitoring

1. Introduction

Located at the coast of Southern China, Hong Kong experiences weather systems coming from the south over the South China Sea in the summer. Such systems include those bringing adverse weather to the territory, such as active southwest monsoon, troughs of low pressure, and tropical cyclones. Even in winter and springtime, weather systems such as northerly wind surges and easterly wind surges associated with the northeast monsoon could bring about significant changes to the weather in Hong Kong and its adjacent waters. As such, weather observations over the seas are very valuable for monitoring the evolution of the weather systems and for ingesting into numerical weather prediction (NWP) models for weather nowcasting and forecasting.

It has long been recognised that the benefits of weather observations over the seas to the south of Hong Kong are for local weather forecasting. In the 1980s, collaboration had already been in place between the weather service of Guangdong province and the Hong Kong Observatory (HKO, the then Royal Observatory) to set up weather stations on the

Check for updates

Received: 9 February 2026
Revised: 30 March 2026
Accepted: 31 March 2026
Published: 3 April 2026

Copyright: © 2026 by the authors. Licensee MDPI, Basel, Switzerland. This article is an open access article distributed under the terms and conditions of the Creative Commons Attribution (CC BY) license.

islands over the South China coastal waters, including Huangmao Zhou. More weather stations have been set up over the islands and offshore waters of Guangdong since then. In the 2010s, the mainland China side also set up weather stations at the oil rigs over the South China Sea and deployed weather buoys over its northern part for real-time data transmission. HKO also has regular deployment of drifting buoys in the region since June 2015, with the assistance of Hong Kong Voluntary Observing Ship (HKVOS) [1]. Despite all these efforts, the availability of more frequently updated and densely distributed weather observations, particularly surface winds and significant height of sea waves, is still required, especially over the coastal waters of Guangdong in order to monitor the weather systems coming close to the Guangdong–Hong Kong–Macao Greater Bay Area, which is one of the most densely populated and urbanised regions in the world.

Ground-based remote sensing observations of winds and waves may be an option to fill in the data gaps, such as the use of ocean radar. The research on this kind of radar in Hong Kong, called CODAR (coastal radar system measuring the ocean current), was conducted back in the 1990s/2000s [2]. It has been reported that similar CODARs are in use for the coastal areas of the U.S., Canada and Australia. However, publications about the observations of these systems are rather limited, especially in the application of the monitoring of coastal severe weather systems. One possible reason may be that this kind of high-frequency radar is mainly designed to observe sea current as the primary product, with wave height and wind speed/direction as secondary products, which do not seem to have satisfactory quality persistently. In 2017, HKO also tried to explore this technology by setting up an ocean radar in Hong Kong. Together with the ocean radar at Shanwei, Guangdong, China, this pair of radars could be used to derive sea current speed/direction, wave height and sea surface wind speed/direction. Through continuous effort of hardware and software enhancements, the wind observations are found to have persistently satisfactory quality, providing valuable and unprecedented observations of severe weather systems over the coastal waters to the east of Hong Kong, but still with some limitations.

This paper documents the enhancements to the hardware and software of the ocean radar being implemented so far, studies the performance of the radar's observations by comparing with moored weather buoy observations over an extended period of time, presents some interesting observations of the severe weather systems over the coastal waters, and discusses the limitations of the existing technology and the need of further studies. The authors consider that the enhancements are significant and should be of interest to other developers and users of similar technologies.

2. Ocean Radar Hardware and Setup

The hardware of the ocean radar in Hong Kong (OSMAR071G system) is shown in Figure 1a. It consists of a 3-element Yagi-Uda transmitting antenna, an array of eight whip-type receiving antennas, and a control room for housing a signal transmitter, a signal receiver, and a radar control unit. The radar is operated at an allocated frequency of 5.275 MHz, with a detection depth of approximately 2.5 m, which corresponds to the theoretical value of $\lambda/8\pi$, where λ denotes the transmitted wavelength. Some technical information about the system could be found in ref. [3].

Each of the two ocean radars (in Hong Kong and in Shanwei, technical specifications in Table 1) scans a conical area (Figure 1b). The overlapping area has a size of about 40,000 km^2, and only in this area the observations such as wind, current and wave would be available. A real-time display of the ocean radar data is shown in Figure 1c. Within this area, there are two moored weather buoys, including MF14002 and MF14008 (locations in Figure 1c), providing 10 m high wind speed direction, sea surface current speed and

direction at a depth of 2.5 m, as well as the height of the sea wave. The data from these two buoys would be used in the later section for comparison with the ocean radar observations. There are no other observations, such as weather stations over the islands, that could be available for this verification purpose.

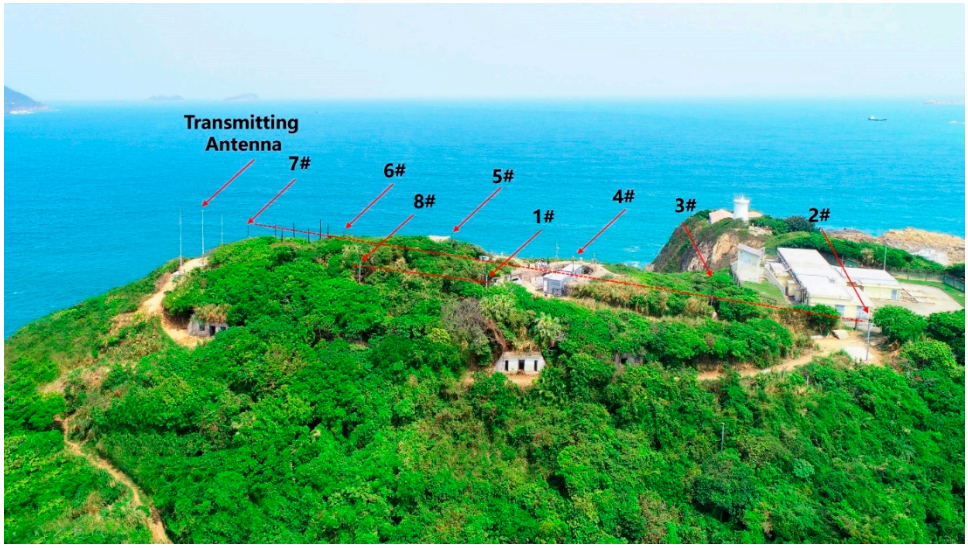

(**a**)

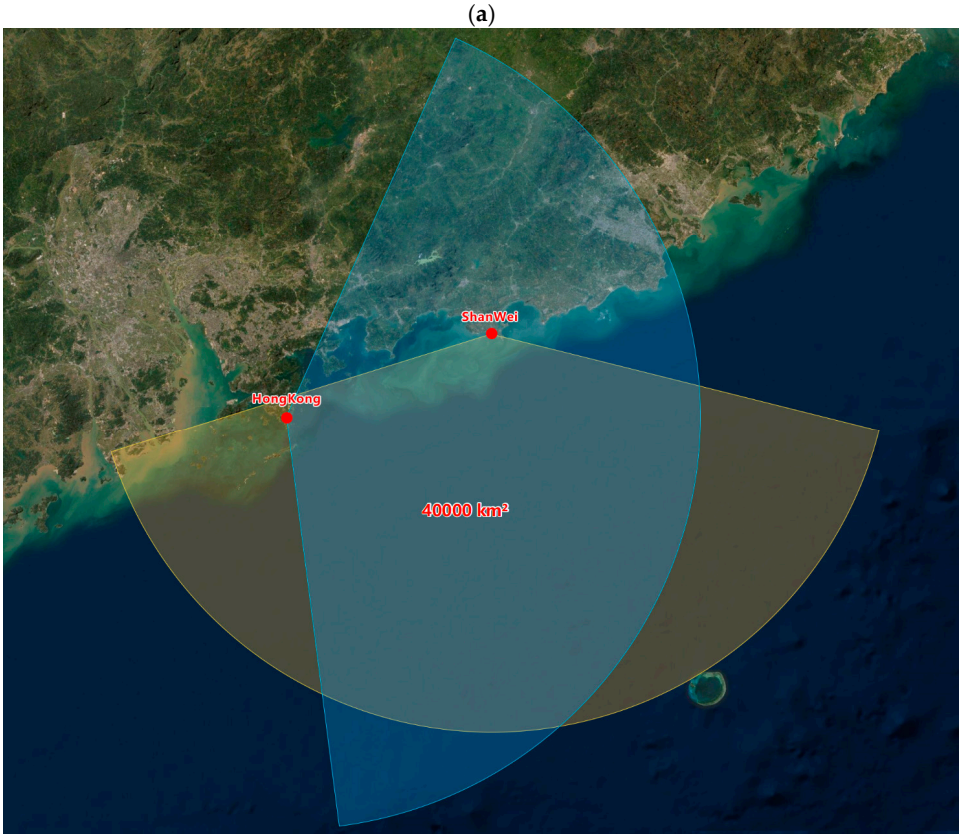

(**b**)

Figure 1. *Cont.*

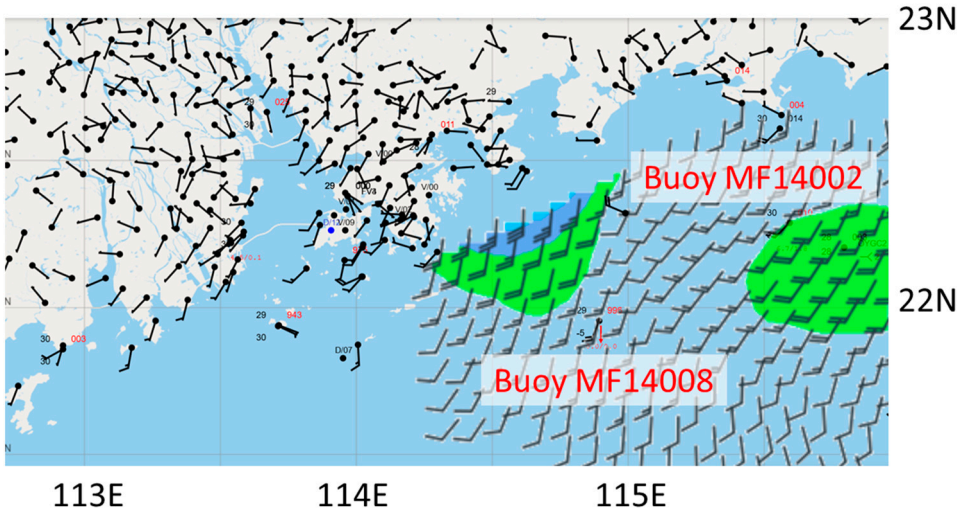

(c)

Figure 1. (**a**) The antenna setup of the ocean radar in Cape D'Aguilar in Hong Kong with 1# to 8# indicating the position of the eight receiving antennas; (**b**) the coverage of the Hong Kong–Shanwei radar pair; and (**c**) sample wind data and weather observations nearby. The approximate location of the two buoys (MF14008 and MF14002) used in this study is also shown.

Table 1. Technical parameters of the OSMAR in Hong Kong and Shanwei.

Station Name	Hong Kong Station	Shanwei Station
Main frequency of radar	~5.275 MHz	~5.59 MHz
Sweep bandwidth	30 KHz	30 KHz
Sweep period	0.6528 s	0.6528 s
Array normal direction	178.88°(relative to true north)	98°(relative to true north)
Range resolution	5 km	5 km
Angle resolution	1.5°	1.5°
Detection range	300 km	300 km
Temporal resolution	10 min	10 min

3. Retrieval Software Algorithm

The software algorithm consists of ocean current inversion, wind inversion and wave inversion. The radial current towards or away from a radar station is obtained through single-radar detection inversion, and then the vector current is synthesised based on the radial current data obtained by two radars. For the wind and wave inversion algorithm, the wind direction and wind speed are firstly inverted using the energy ratio and the spread factor of the first-order peak of the radar Doppler spectrum, then deblurring is performed via dual-station processing, and finally wave parameters are inverted combined with the empirical wind model. The various inversion algorithms are briefly described in the following paragraphs.

3.1. Ocean Current Inversion Algorithm

Ocean current inversion with high-frequency surface wave radar includes single-station radial current inversion and dual-station vector current inversion. In single-station inversion, the detection area is divided into range bins and azimuth bins. The signal processing flow is as follows: first, perform the fast Fourier transform (FFT) on the frequency-swept

echo to obtain the complex-valued signal of each range bin; then correct errors using the amplitude–phase calibration factor, process the data in overlapping segments, and generate a snapshot receiving matrix through short-time Fourier transform (STFT); subsequently, perform a second-order FFT on the samples of each range bin to generate an omnidirectional Doppler spectrum, reduce noise through multi-antenna snapshot averaging, and separate the first-order spectral region using the difference spectrum method (only the spectral points in this region are used for current measurement); further, according to the first-order scattering theory of Barrick [4], the frequency offset in the first-order spectral region has a specific relationship with the radial velocity.

$$f_{dpl_radial} = f_{dpl} - f_{dpl_bragg}$$

The radial velocity is derived from the Doppler relationship:

$$V_{radial} = \frac{\lambda \cdot f_{dpl_radial}}{2}$$

where λ is the radar wavelength, and f_{dpl_bragg} is the Bragg wave frequency offset without current (with positive/negative values corresponding to waves approaching/away from the radar); finally, for spectral points with SNR > 6 dB, the multiple signal classification (MUSIC) algorithm is used to estimate the direction of arrival (DOA) (the number of signal sources must be accurately estimated first) to determine the azimuth of the range bin corresponding to the radial current velocity [5–7].

For dual-station inversion of vector current, a Cartesian coordinate system (Figure 2a) is established with radar station 1 as the origin, the line connecting the two stations as the x-axis, and its perpendicular as the y-axis. For a point $P(x, y)$ in the common detection area, let its velocity magnitude be V and direction be θ (the angle increases counterclockwise from the positive x-axis). The radial velocities measured by radar stations 1 and 2 are V_1 (direction ξ_1) and V_2 (direction ξ_2), respectively. According to the geometric relationship, the radial velocity and vector velocity satisfy:

$$V_1 = V\cos(\theta - \xi_1)$$

$$V_2 = V\cos(\theta - \xi_2)$$

The position of point P is solved using geometric methods: Let the distances from the two stations to point P be r_1 and r_2, then

$$r_1 = \frac{2d\sin(\pi - \xi_2)}{\sin(\xi_2 - \xi_1)}$$

$$r_2 = \frac{2d\sin(\xi_1)}{\sin(\xi_2 - \xi_1)}$$

(where d is the distance between the two stations). The area of the triangle is $S = dr_1\sin\xi_1$, so the coordinates of point P are:

$$y = \frac{S}{d}$$

$$x = d - \sqrt{r_2^2 - y^2}$$

By combining the radial velocity formulas, the velocity magnitude and direction of point P are obtained:

$$\theta = \arctan\left(\frac{V_2\cos\theta_1 - V_1\cos\theta_2}{V_1\sin\theta_2 - V_2\sin\theta_1}\right)$$

$$V = \frac{V_1}{\cos(\theta - \xi_1)}$$

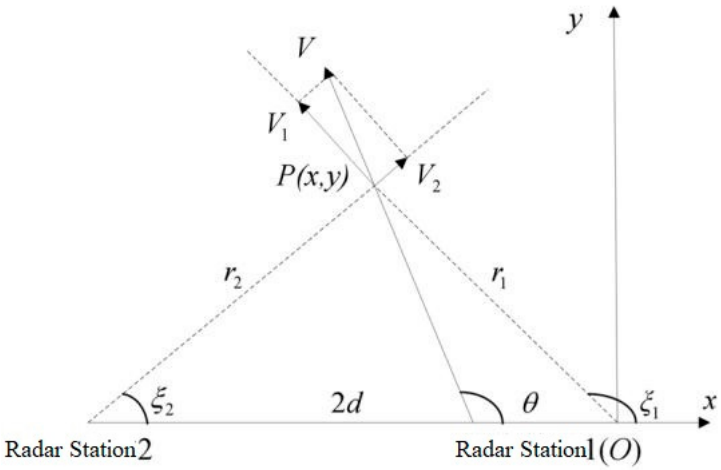

(**a**)

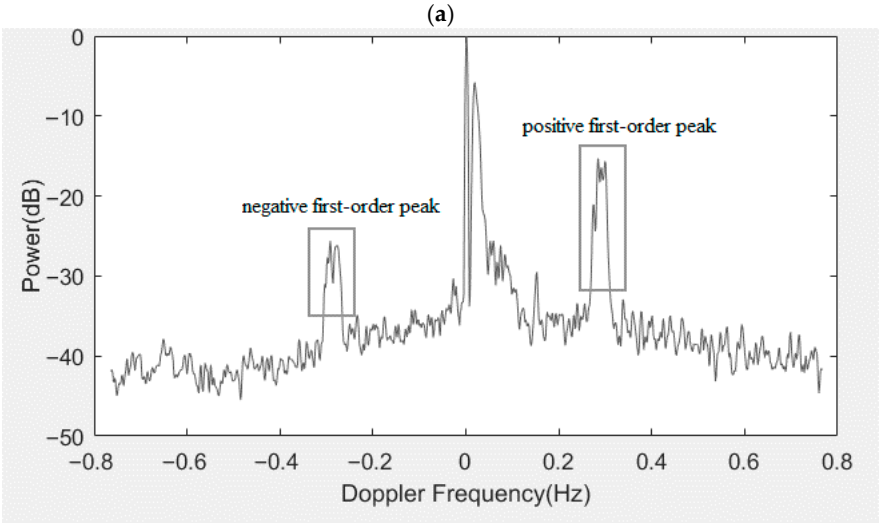

(**b**)

Figure 2. Geometry of the measurement point with respect to the two radar stations (**a**) and the sample power spectrum (**b**).

3.2. Wind and Wave Inversion

Barrick [4,8,9] used the perturbation method to quantitatively describe the formation mechanism of first-order ocean echoes on rough sea surfaces and gave the first-order scattering cross-section equation:

$$\sigma_1(\omega) = 2^6 \pi k_0^4 \sum_{m=\pm 1} S\left(-2m\vec{k}\right)\delta(\omega - m\omega_B)$$

where k_0 is the wave number (in rad/m), ω is the angular frequency (in rad/s), and ω_B is the Bragg wave angular frequency (in rad/s). Bragg waves are waves with a wavelength equal to half of the radio wave wavelength, propagating along the beam direction towards or away from the radar. The echo generated by the backscattering of Bragg waves is called the first-order ocean echo. m is the sign of the Doppler frequency; a positive sign indicates that the Bragg wave approaches the radar along the beam direction, called a positive Bragg wave; a negative sign indicates that the Bragg wave moves away from the radar along the beam direction, called a negative Bragg wave. k is the wave vector, and $S(k)$ represents the radar directional spectrum.

Therefore, for any detection range bin, the ratio of the power spectra of the positive and negative first-order peak ocean echoes (Figure 2b) is:

$$R = \frac{\sigma_1^+(\omega_B)}{\sigma_1^-(\omega_B)} = \frac{S(-2mk)}{S(2mk)}$$

$S(k)$ can be expressed as the product of the isotropic wave height spectrum $S(k)$ and the directional factor $G(\theta)$. Assuming the radar beam direction is θ_0, then:

$$R = \frac{G(\theta_0 + \pi)}{G(\theta_0)}$$

Using the cosine model proposed by Longuet-Higgins [10,11] as the directional factor function:

$$G(\theta_0) = \cos^S\left(\frac{|\theta_w - \theta_0|}{2}\right)$$

where θ_w is the wind direction. Further, we can obtain:

$$R = \tan^S\left(\frac{|\theta_w - \theta_0|}{2}\right)$$

The logarithmic form is as follows:

$$R_{dB} = 10S\log_{10}\left(\tan\left(\frac{|\theta_w - \theta_0|}{2}\right)\right)$$

The OSMAR071G high-frequency surface wave radar is a wide-beam radar system. It uses the MUSIC algorithm [5–7] to realise Bragg wave azimuth estimation, and then performs beamforming by aligning these azimuths using minimum variance distortionless response (MVDR) [12,13] to estimate the echo power density of Bragg waves. Two-dimensional spatial fitting of the power densities of positive and negative Bragg wave echoes within the radar detection range can obtain their continuous distribution over the entire detection range, and then the positive/negative first-order peak power ratio R_{dB} at any position can be derived.

Under the condition of single-radar detection, it is easy to derive from the above formula that:

$$\theta_w = \theta_0 \pm 2\arctan\left(\left(\frac{\sigma_1^+}{\sigma_1^-}\right)^{\frac{1}{S}}\right)$$

For single-radar detection, the inversion of wind direction has ambiguity.

The OSMAR071G high-frequency surface wave radar uses dual-station (multi-station) processing for deblurring and performs joint estimation of wind direction and wind direction spread factor. A cost function is constructed:

$$LSM(S, \phi_w) = \sum_{i=1}^{M}\left(R_{dB_i} - 10S_i\log 10\left(\tan\left(\frac{|\phi_w - \phi_i|}{2}\right)\right)\right)^2$$

M represents the number of stations, typically $M = 2$. i denotes the station index. R_i is the ratio of positive and negative first-order peaks at the detection point for station i, and ϕ_i is the beam angle (in degrees). ϕ_w is the wind direction (in degrees), and S_i is the spread factor.

There is only one true wind direction. Theoretically, for the above formula, the closer S and ϕ_w are to their true values, the smaller $LSM(S, \phi_w)$ is. By minimising $LSM(S, \phi_w)$ the deblurred wind direction and wind direction spread factor can be estimated.

The formula used in the study of Mitsuyasu [14] quantitatively describes the relationship between the wind direction spread factor and wind speed. The spread factor measured by high-frequency surface wave radar is an average result over the entire range bin, and there is a significant difference in value from the result measured by buoys in the formula. However, the physical meaning of the spread factor measured by the radar should conform to the relationship described by Mitsuyasu [14]. Therefore, the OSMAR071G high-frequency surface wave radar system in Hong Kong–Shanwei re-fitted the functional relationship between the spread factor and wind speed based on the measured wind speed from buoys, expressed as:

$$\begin{cases} S = 1.703\frac{2\pi f_B}{g}U & \text{(rising segment)} \\ S = 12.169\left(\frac{2\pi f_B}{g}\right)^{-1.966}U^{-1.966} & \text{(falling segment)} \end{cases}$$

where U is the wind speed (in m/s), f_B is the Bragg wave frequency (in Hz), and g is the gravitational acceleration (in m/s^2).

Wave height data from high-frequency surface wave radar is obtained via wind speed inversion. Its physical basis lies in the fact that ocean waves are mostly generated by wind-driven forces, and there is a significant correlation between wind speed and wave height.

By analysing, correcting and fitting buoy-measured data, the following empirical wave height inversion formula can be established:

$$Wave = 0.007839 \times Wind^{2.118} + 0.6645$$

In the formula, *Wave* denotes wave height (in m), and *Wind* denotes wind speed (in m/s). The coefficients of this formula are derived from nonlinear regression fitting of historical datasets. Retaining multiple significant figures is intended to mathematically describe the statistical relationship between wind and waves more accurately. In operational applications, the wind speed (*Wind*) input values retrieved by the radar inherently carry a certain degree of uncertainty, with a typical error range of approximately ± 1 to 2 m/s. Propagating this input uncertainty through the nonlinear formula yields a typical uncertainty in the corresponding wave height (*Wave*) output of approximately ± 0.2 to 0.5 m (the exact magnitude varies with wind speed). This formula can relatively accurately invert wave height values based on wind speed, providing an effective approach for high-frequency surface wave radar to obtain wave heights in marine monitoring.

4. Comparison with Buoy Observations

The moored weather buoys MF14002 and MF14008 (locations in Figure 1c) are used to examine the quality of observations from the ocean radar, including wind speed, wind direction, wave height, sea current speed and sea current direction (for MF14002 only because the sea current direction observations from MF14008 suffer from problems with the magnetization of the buoy hull). The scatter plots, best-fit equations to the data points and the coefficient of determination (R^2) are given in Figures 3 and 4 for MF14002 and MF14008, respectively. The error statistics, namely, mean difference, mean absolute difference and root-mean-square difference, as well as the distribution of the differences across the whole range for the two buoys, are shown in Tables 2 and 3. The 95% confidence intervals (the 2.5th and 97.5th percentiles of the bootstrap distribution as the lower and upper bounds, respectively) for all error metrics were also computed using non-parametric bootstrap resampling with the percentile method [15,16] and with 10,000 iterations. A systematic comparison over a period of one year, from June 2024 to July 2025, covers different seasons

and thus wind directions (northeast monsoon in the winter, and southwest monsoon in the summer) and includes different types of weather scenarios (monsoon surges, troughs of low pressure, tropical cyclones, etc., as discussed in the following section).

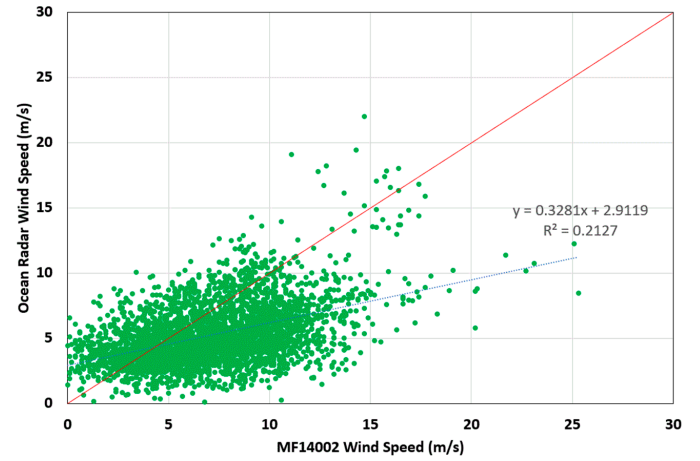

(**a**)

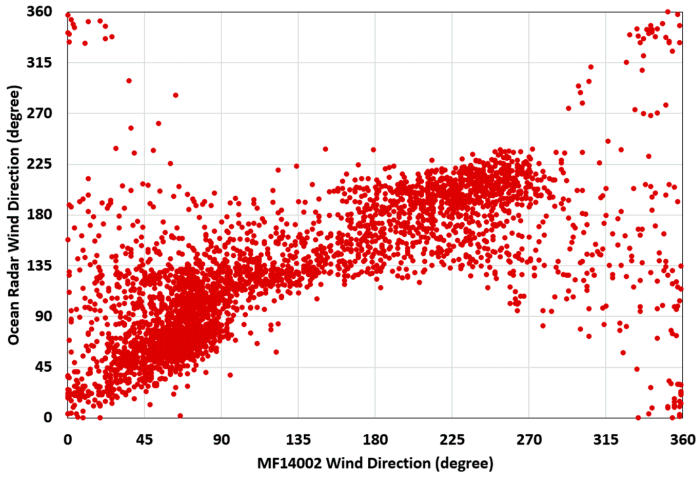

(**b**)

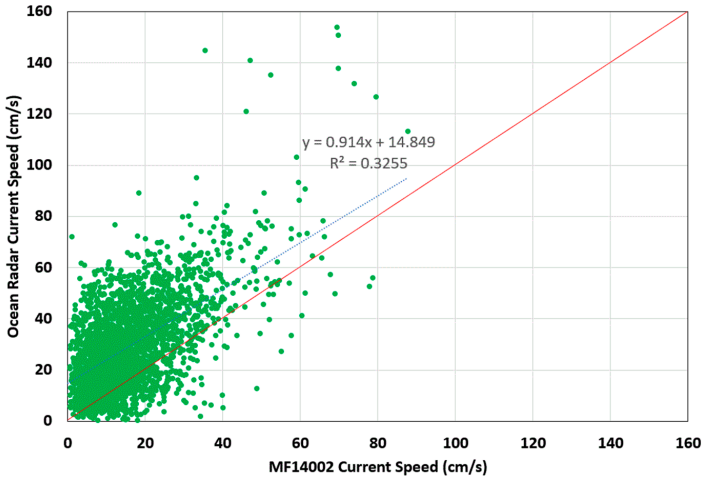

(**c**)

Figure 3. *Cont.*

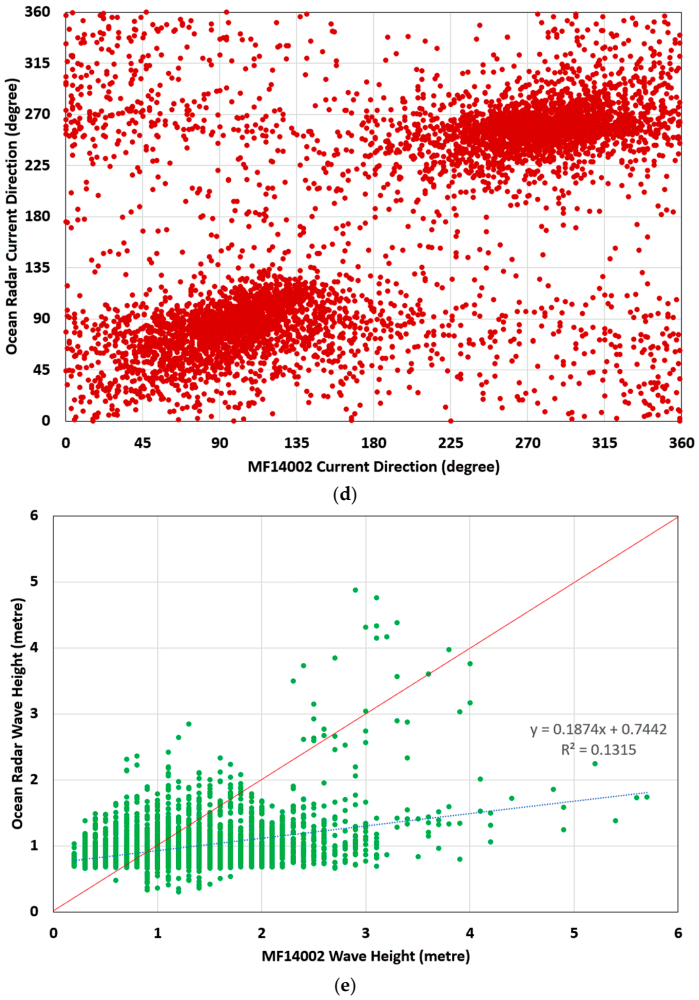

Figure 3. Comparison between buoy MF14002 data (x-axis) and ocean radar outputs (y-axis) of (**a**) wind speed; (**b**) wind direction; (**c**) current speed; (**d**) current direction; and (**e**) significant wave height from June 2024 to July 2025. The red line in (**a**,**c**,**e**) shows perfect agreement (x = y).

There are a number of observations:

(1) The correlation between ocean radar wind speed/wave height and buoy observations of MF14008 (R = 0.69/0.55) is significantly higher than that of MF14002 (R = 0.55/0.36). It is reasonable as the MF14008 lies in the core region of the central overlapping area of the two ocean radars, while MF14002 lies closer to the coast outside the core region.

(2) For wind speed, according to the World Meteorological Organization publication No. 8 [17], the required measurement uncertainty is 0.5 m/s for ≤5 m/s, 10% for >5 m/s. Based on a wind speed of 10 m/s, the uncertainty is 1 m/s. The mean absolute difference in ocean radar wind speed is generally 2–3 times the measurement uncertainty. From the mean difference in Tables 2a and 3a and the distribution of differences in Tables 2b and 3b, the ocean radar wind speed generally shows a systematic underestimation. The narrow confidence intervals reflect the large sample size and consistent measurement performance across the validation period. The correlation between ocean radar wind speed and buoy observation at MF14008 is the highest (with R^2 = 0.47 or R = 0.69) among all elements. Its correlation is even higher than that of the current speed, with R^2 = 0.33 or R = 0.57. It is likely that the positive result is due to calibration and optimisation with a focus on improving the accuracy of ocean radar wind observations. The ocean radar wind speed is still con-

sidered useful for operation, with the understanding that wind speed is the secondary derived product.

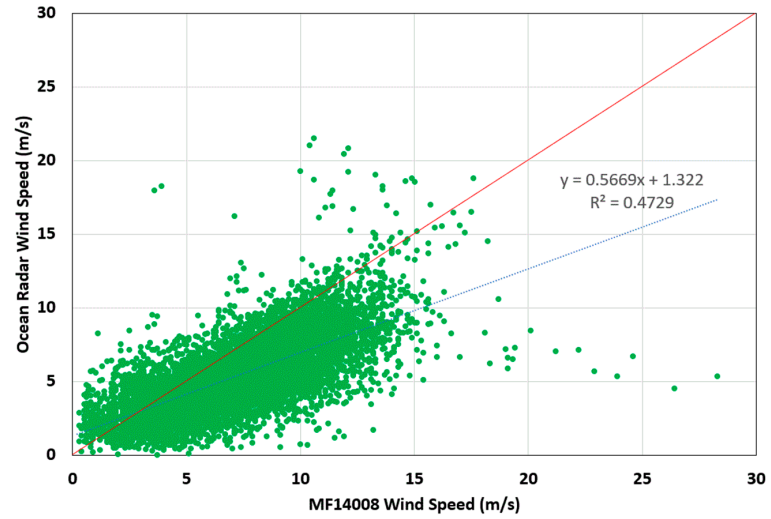

(a)

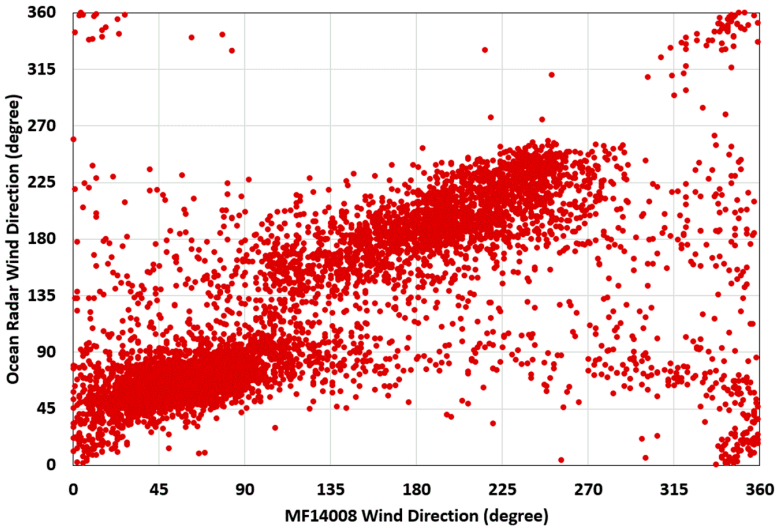

(b)

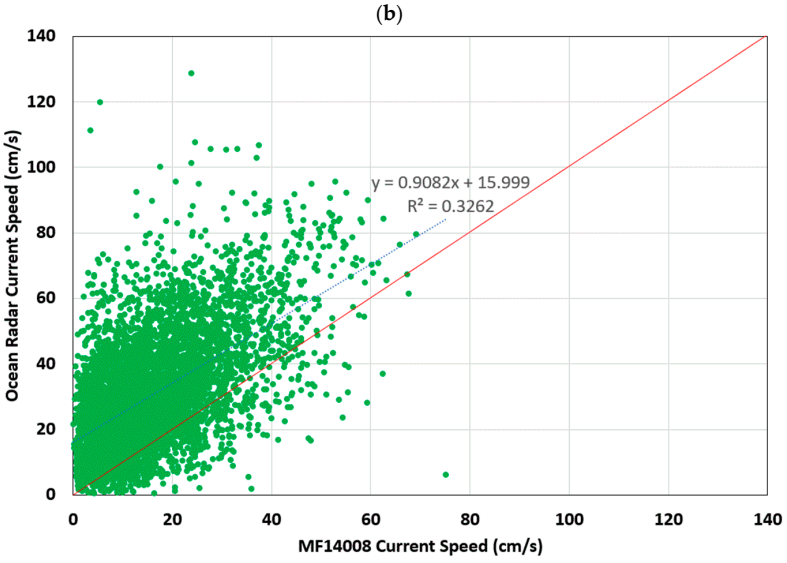

(c)

Figure 4. *Cont.*

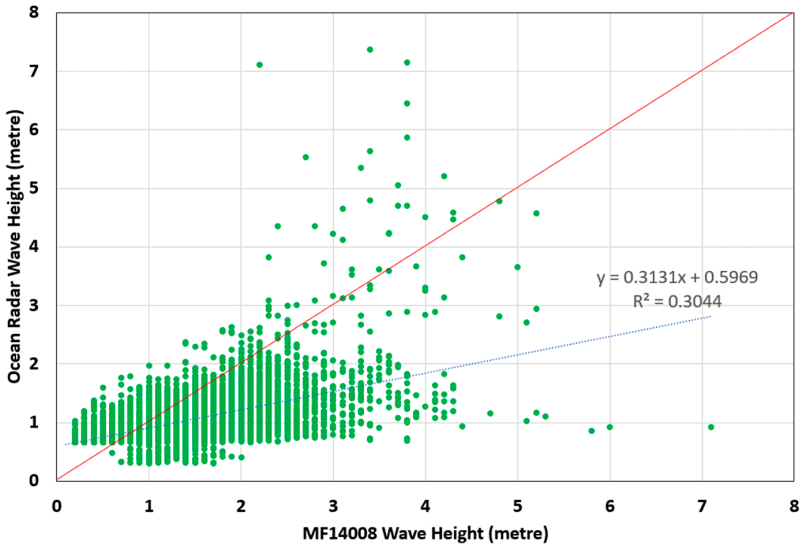

(**d**)

Figure 4. Comparison between buoy MF14008 data and ocean radar outputs of (**a**) wind speed; (**b**) wind direction; (**c**) current speed; and (**d**) significant wave height from June 2024 to July 2025. The red line in (**a**,**c**,**d**) shows perfect agreement (x = y).

Table 2. (**a**). Performance of ocean radar observation as compared with the buoy MF14002 from June 2024 to July 2025. The difference refers to ocean radar data minus buoy data. The figures in square brackets show the 95% confidence interval estimated using the percentile bootstrap method. (**b**). Distribution of the differences between ocean radar data and observations of the buoy MF14002 from June 2024 to July 2025. The difference refers to ocean radar data minus buoy data.

(**a**)

	Wind Speed	Wind Direction	Wave Height	Current Speed
Mean difference	−1.85 m/s [−1.95, −1.75]	36.36 degrees [35.15, 37.62]	−0.28 m [−0.30, −0.26]	12.29 cm/s [11.91, 12.66]
Mean absolute difference	2.82 m/s [2.74, 2.89]	36.36 degrees [35.15, 37.62]	0.56 m [0.54, 0.58]	14.96 cm/s [14.66, 15.27]
Root-mean-square difference	3.56 m/s [3.47, 3.65]	51.87 degrees [50.13, 53.60]	0.73 m [0.70, 0.75]	19.04 cm/s [18.65, 19.43]

(**b**)

Difference in Wind Speed (m/s)		Difference in Wind Direction (Degree)		Difference in Wave Height (m)		Difference in Current Speed (cm/s)	
Range	**% of Samples**	**Range**	**% of Samples**	**Range**	**% of Samples**	**Range**	**% of Samples**
≤−8	2.5%	0 to 15	34.3%	≤−2	1.4%	≤−45	0.0%
−8 to −6	6.4%	15 to 30	23.8%	−2 to −1.5	2.8%	−45 to −30	0.3%
−6 to −4	15.1%	30 to 45	14.3%	−1.5 to −1	9.0%	−30 to −15	1.7%
−4 to −2	22.9%	45 to 60	9.0%	−1 to −0.5	22.5%	−15 to 0	17.2%
−2 to 0	25.5%	60 to 75	5.8%	−0.5 to 0	25.2%	0 to 15	40.4%
0 to 2	18.1%	75 to 90	3.5%	0 to 0.5	30.6%	15 to 30	29.3%
2 to 4	7.7%	90 to 105	2.5%	0.5 to 1	7.9%	30 to 45	9.6%
4 to 6	1.7%	105 to 120	1.7%	1 to 1.5	0.6%	>45	1.6%
6 to 8	0.3%	120 to 135	1.1%	1.5 to 2	0.1%		
>8	0.0%	135 to 150	1.3%	≥2	0.0%		
		150 to 165	1.3%				
		>165	1.3%				

Table 3. (**a**). Same as Table 2a but for buoy MF14008. (**b**). Same as Table 2b but for buoy MF14008.

(**a**)

	Wind Speed	**Wind Direction**	**Wave Height**	**Current Speed**
Mean difference	−1.85 m/s [−1.90, −1.80]	25.53 degrees [24.84, 26.20]	−0.34 m [−0.35, −0.33]	14.54 cm/s [14.18, 14.91]
Mean absolute difference	2.33 m/s [2.29, 2.37]	25.53 degrees [24.84, 26.20]	0.53 m [0.52, 0.54]	15.99 cm/s [15.68, 16.31]
Root-mean-square difference	2.95 m/s [2.89, 3.01]	40.29 degrees [39.11, 41.47]	0.71 m [0.69, 0.72]	20.32 cm/s [19.90, 20.74]

(**b**)

Difference in Wind Speed (m/s)		**Difference in Wind Direction (Degree)**		**Difference in Wave Height (m)**		**Difference in Current Speed (cm/s)**	
Range	**% of Samples**	**Range**	**% of Samples**	**Range**	**% of Samples**	**Range**	**% of Samples**
≤−8	0.7%	0 to 15	49.8%	≤−2	1.1%	≤−45	0.1%
−8 to −6	2.6%	15 to 30	24.8%	−2 to −1.5	2.7%	−45 to −30	0.8%
−6 to −4	12.3%	30 to 45	10.6%	−1.5 to −1	9.6%	−30 to −15	11.6%
−4 to −2	30.5%	45 to 60	4.8%	−1 to −0.5	23.4%	−15 to 0	44.3%
−2 to 0	34.3%	60 to 75	2.8%	−0.5 to 0	29.9%	0 to 15	29.8%
0 to 2	16.2%	75 to 90	1.8%	0 to 0.5	29.5%	15 to 30	10.6%
2 to 4	2.8%	90 to 105	1.1%	0.5 to 1	3.6%	30 to 45	2.2%
4 to 6	0.4%	105 to 120	1.1%	1 to 1.5	0.1%	>45	0.6%
6 to 8	0.1%	120 to 135	0.9%	1.5 to 2	0.0%		
>8	0.1%	135 to 150	0.8%	≥2	0.1%		
		150 to 165	0.7%				
		>165	0.7%				

(3) For wind direction, the uncertainty requirement of WMO is 5 degrees. The wind direction differences in ocean radar data are generally around 20–40 degrees, significantly higher than the measurement uncertainty. Apparently, there is a systematic positive difference in ocean radar wind direction, i.e., clockwise from the buoy. The width of the confidence interval for the buoy MF14008 is about half that of MF14002, indicating more consistent directional measurements. In fact, around 75% of the ocean radar wind direction is within 30 degrees of the buoy MF14008 in the core region of the central overlapping area of the ocean radar pair.

(4) For wave height, the WMO requirement of measurement uncertainty is 0.5 m for ≤5 m, 10% for >5 m. The mean absolute difference of 0.5–0.6 m for ocean radar wave data is comparable to the measurement uncertainty. Around 86% of the ocean radar wave height data is within 1 m of the buoy data. However, the correlation between ocean radar wave data and buoy observations is the lowest, with a correlation of only 0.36–0.55.

(5) For sea current speed, the uncertainty is taken to be 7 cm/s [18,19]. The mean absolute difference of about 15 cm/s for ocean radar current is around two times the uncertainty. However, the root-mean-square difference of around 20 cm/s is actually comparable to the operational accuracy reported for typical HF radar systems in the Zhoushan Sea region (15–25 cm/s) [18], demonstrating the validity and engineering practicality of our retrieval method.

The relatively lower accuracy of wave height and sea current speed retrievals compared to wind parameters can be attributed to several inherent physical and methodological challenges in HF ocean radar remote sensing, which are briefly explained below.

For wave height retrieval, the primary limitation lies in the weak signal strength of the second-order sea echoes, which are typically 10–20 dB lower than that of the first-order Bragg peaks. Under low sea states or calm conditions, the second-order spectral energy becomes extremely weak and may be completely buried in system noise and interference, making reliable extraction difficult. Furthermore, actual sea waves represent a complex superposition of wind waves (locally generated) and swell (propagated from distant sources), often exhibiting multi-peak directional spectra. However, most inversion algorithms assume a single wind–wave spectral peak under "fully developed" sea conditions. When swell energy dominates, particularly during low sea states or transitional conditions, the radar-observed spectral characteristics reflect mixed energy contributions. Applying pure wind–wave models in such cases erroneously attributes swell contributions to local wind forcing, leading to systematic biases in both retrieved wave height and wind speed. This explains the wave height underestimation and increased errors observed in low wind speed intervals in our results.

Additionally, wave height retrieval suffers from error propagation along the inversion chain. Whether through traditional second-order spectral methods or modern first-order peak spreading factor approaches, wave height typically represents the final output in the retrieval sequence. Its accuracy depends on the precision of preceding wind speed retrievals and the validity of localised wind–wave relationship models, creating cumulative error effects. Physical saturation effects also constrain retrieval performance: Bragg-resonant wave energy saturates at higher wind speeds (e.g., >15 m/s), becoming insensitive to further wind increases [20]. This saturation limits the effectiveness of spreading factor or energy-based methods in high sea states, such as near the eye walls of typhoons.

Regarding the sea current retrieval, the accuracy of vector current depends not only on radial current inversion algorithms, but also significantly on the radar site geometry. The sea current speed errors can be partly attributed to geometric dilution of precision (GDOP) effects [21]. The two buoys are positioned relatively close to the shore near individual radar stations, whereas the optimal measurement region lies in the central overlapping area where the two radar beams intersect at favourable angles.

Given the above, if wind speed and wind direction are of major concern for meteorological applications, the quality of the ocean radar data in these two aspects are considered to be generally acceptable as evident from Table 4 which shows a comparison of the performance of ocean radar wind speed and wind direction over the central overlapping area of the radar pair in this study and the previous studies on HF radar. Further improvements would be required for wave height and sea current speed observations of the ocean radar.

Table 4. Comparison of the performance of ocean radar wind speed and wind direction in various studies.

Study	Meteorological Conditions	Wind Speed Root-Mean-Square Difference	Wind Speed Correlation	Wind Direction Root-Mean-Square Difference	Wind Direction Correlation
This study	June 2024–July 2025, covering all seasons	2.95	0.69	40.3	0.70
[22]	29 January–7 March 2023 (Wind speed > 5 m/s)	1.83	0.71	16.7	0.97
[23]	During Typhoon Chan-Hom in July 2015 (wind speed > 5 m/s)	3.26	0.53	27.0	0.66
[24]	Typhoon cases in 2017–2019 (wind speed > 4.7 m/s)	3.10	0.78	24.9	0.85
[25]	During Typhoon Fung-Wong in July 2008	3.50	0.77	27.7	0.98

It should be noted that the restricted spatial coverage limits the generalisation of the performance results. Although the buoys in this study are located within the radar wind field synthesis area, they are not positioned at the optimal observation locations. The optimal observation region for a dual-station HF radar is generally near the intersection of the two station normals, closer to the inner side of the radar pair, as the echo signal quality is typically better near the radar normal direction. Therefore, the comparison results between the wind field and buoys in this study reflect the detection performance under actual operational conditions, but not the potential best performance achievable in the optimal region.

5. Examples of Wind Observations

The wind observations for four different types of weather conditions are considered in this paper, and they are listed in the sub-sections below.

5.1. Monsoon Surges

Figure 5 shows a case of the arrival of an easterly surge to Hong Kong in April 2024. A sequence of observations at three time instances is given. Though the buoy wind observations do not change much, the wind speed distributions from the ocean radar show the westward spreading of the strong winds, and thus the arrival of stronger easterly winds at Hong Kong. The ocean radar data are useful in monitoring the spread of the easterly surge over the southeastern coast of China.

Figure 6 shows a snapshot of the prevalence of northerly winds in an outbreak of continental flow in January 2025. The main point to note is the terrain effect on the northerly winds as shown from the surface observations over land, which is consistent with the picking up of the northerly winds over the seas to the south. Such a terrain effect on offshore flow has been observed in the past at other places, for instance, synthetic aperture radar (SAR) satellite observations. This is the first time that the effect is clearly demonstrated from ocean radar observations over the South China coast.

5.2. Troughs of Low Pressure

Figure 7 is a situation of the presence of a surface trough of low pressure over the South China coastal waters, with the coast of Guangdong "protected" from the heavy rain by easterly winds, which were relatively dry. Circulating winds are observed by the ocean radar, consistent with weather buoy observations and the location of weather radar echoes (which are independent measurements from the ocean radar). The location of the trough is captured well by the ocean radar, and such information would be crucial in monitoring severe weather near the coast.

Figure 8 is a case of northward migration of the surface trough of low pressure. A sequence of ocean radar and buoy winds at three time instances is shown. The wind direction change following the migration of the trough is captured well by the buoy observation. The northward movement is consistent with the ocean radar wind observations, and in fact, closed circulations have been captured a couple of times by the ocean radar.

5.3. Rainstorms in the Southwest Monsoon

Hong Kong experiences severe rainstorms in August 2025. Snapshots of surface wind observations in the rainstorms of 2 August and 5 August are shown in Figures 9a and 9b, respectively. Overlaid on the surface observations are the weather radar echoes. The ocean radar winds are found to be consistent with the locations of the stronger radar echoes: (1) for radar echoes near Hong Kong, there is troughing flow as shown in the ocean radar; (2) for more intense and widespread radar echoes over eastern coast of Guangdong, there is either a jet or surface convergence (west to northwesterlies from land observations and

south to southerlies from ocean radar winds) over that coastal region as shown in the surface winds; and (3) south of the feature in (2) above, there are basically no weather radar echoes, consistent with the ridging flow in the surface winds from the ocean radar. In general, the ocean radar winds have the potential to be used together with the land-based surface observations to build up a surface analysis wind field in real-time for severe weather monitoring and nowcasting purposes.

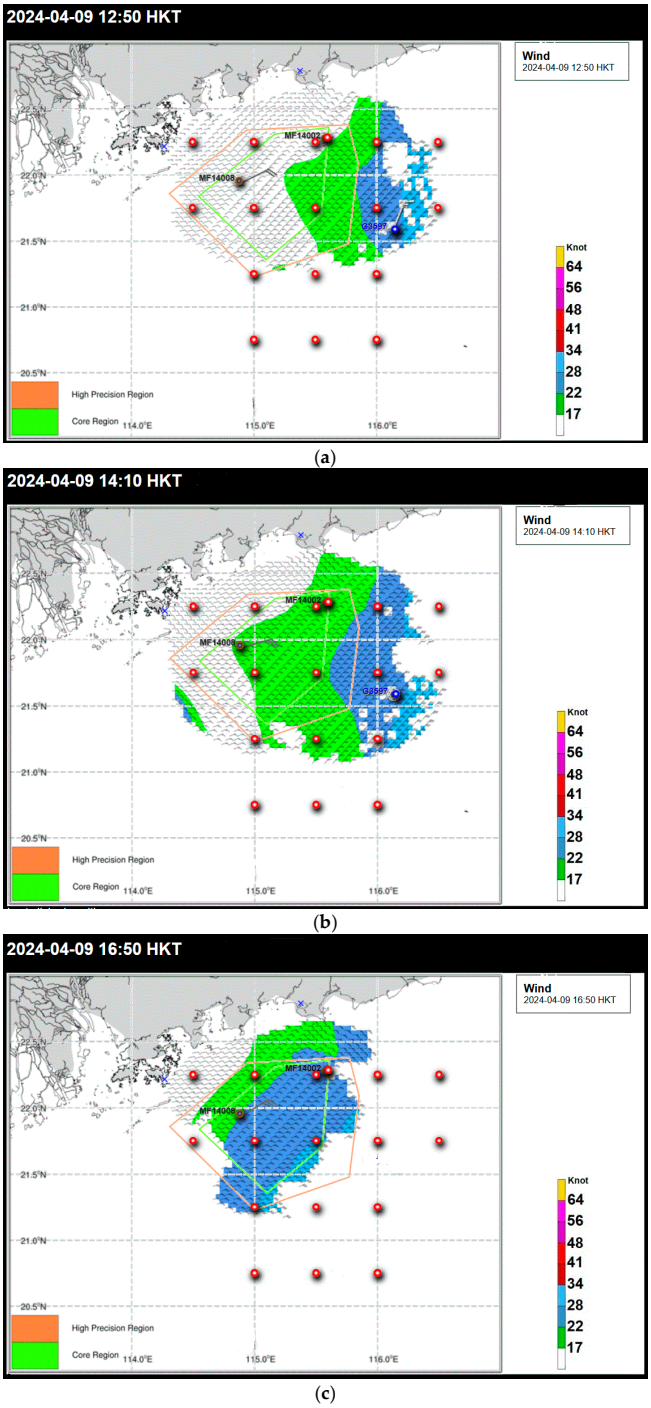

Figure 5. Ocean radar wind output of the wind field for an easterly wind case showing the spreading of strong easterly winds from around 115.8° E in (**a**) to around 115.6° E in (**b**) and then to around 114.8° E in (**c**).

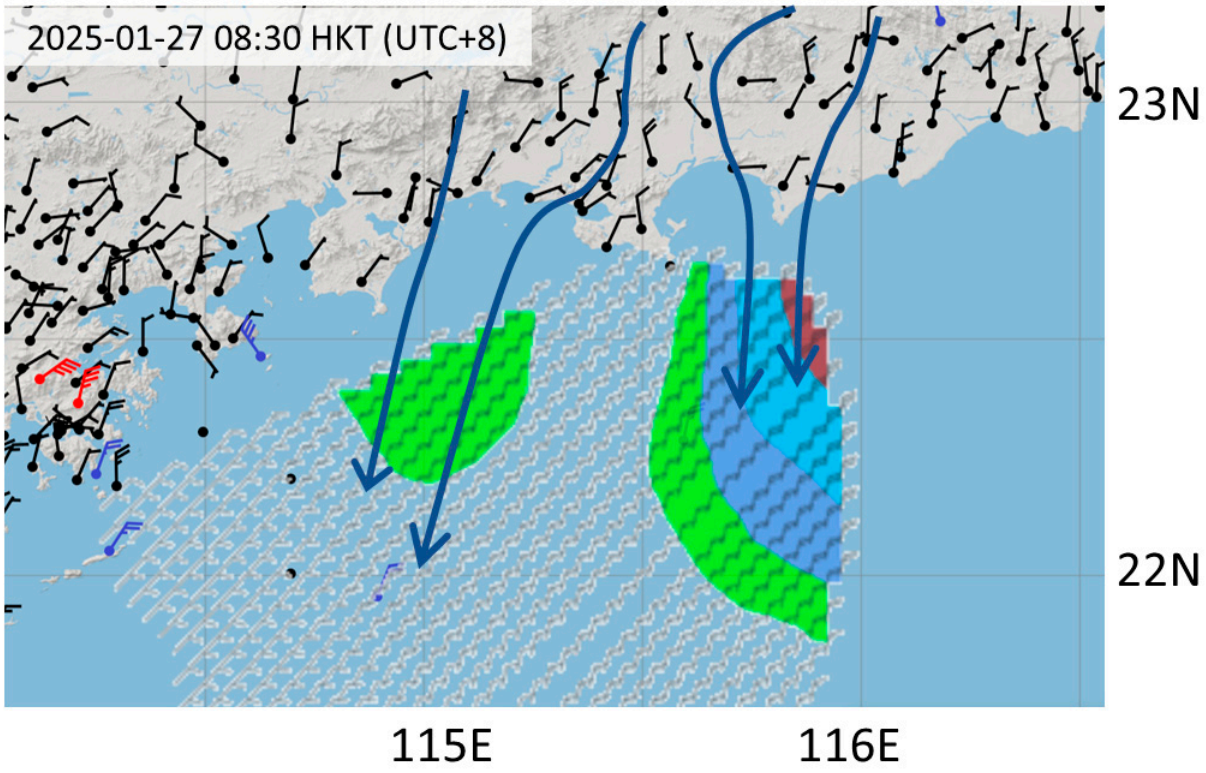

Figure 6. Ocean radar wind output for a northerly wind case.

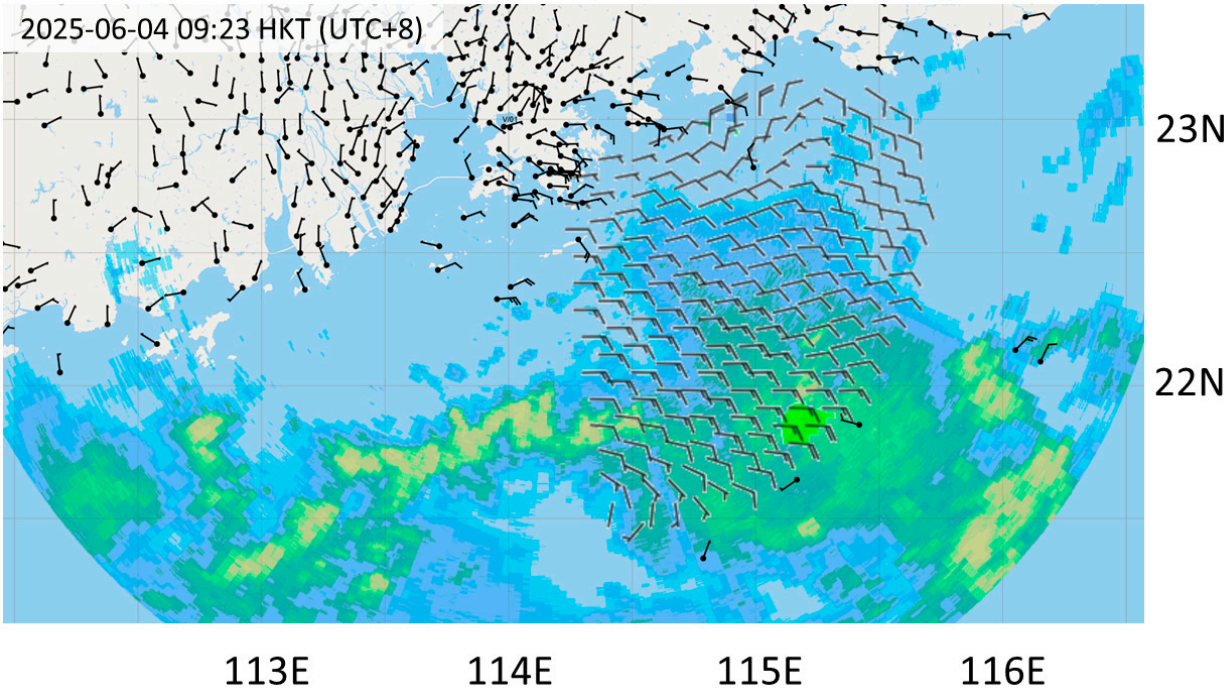

Figure 7. Ocean radar wind output for a surface troughing flow.

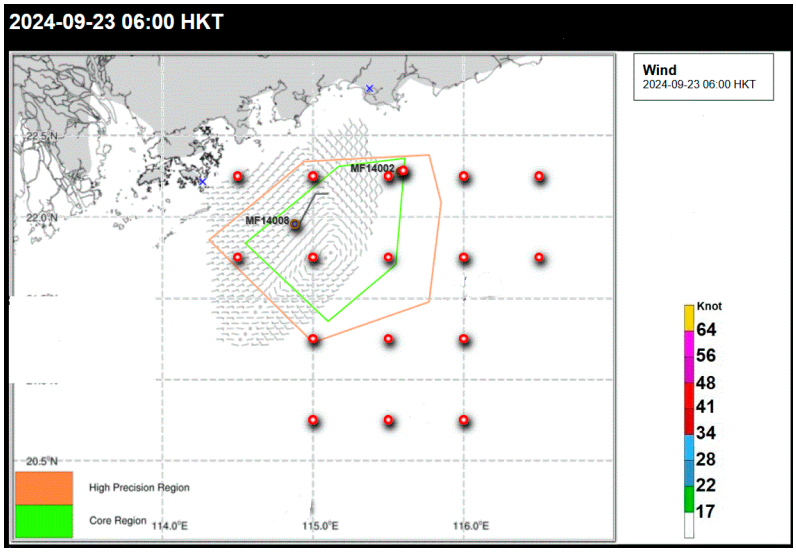

(**a**)

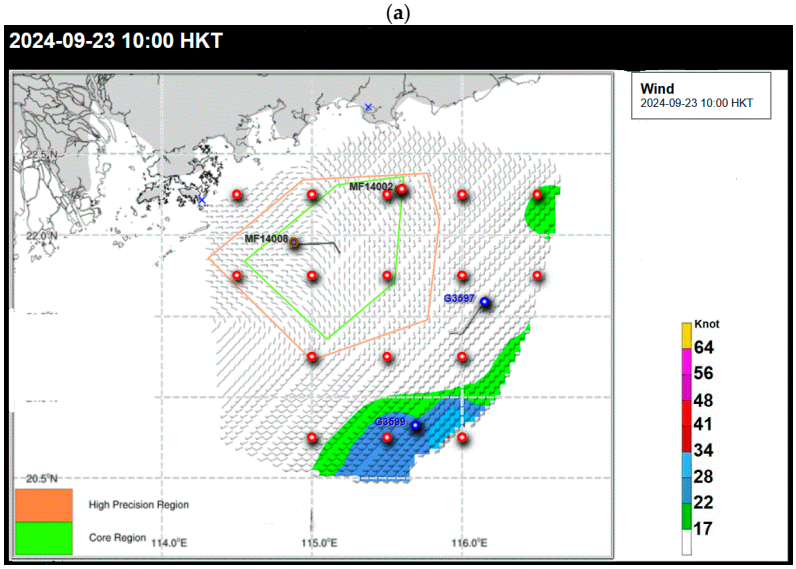

(**b**)

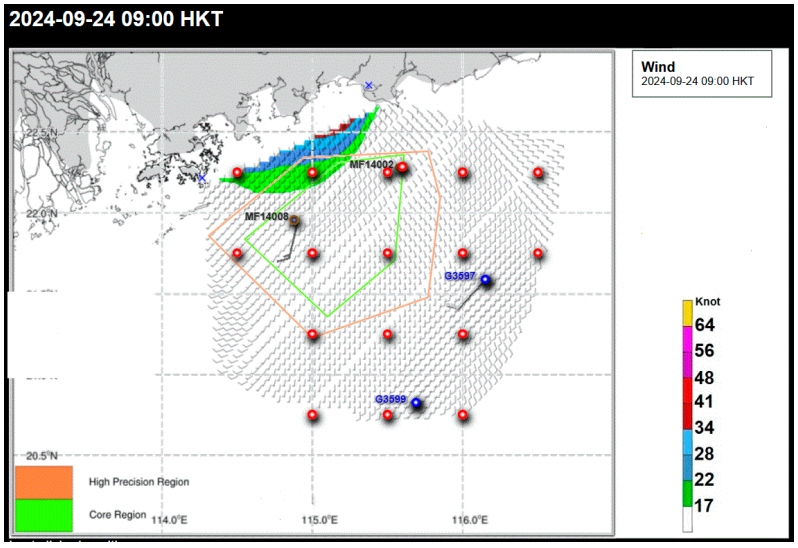

(**c**)

Figure 8. Ocean radar wind outputs overlaid with buoy winds show a surface trough moving north, near 21.6 N in (**a**); around 21.8 N in (**b**) and then near 22.0 N in (**c**), gradually towards the coast of southern China.

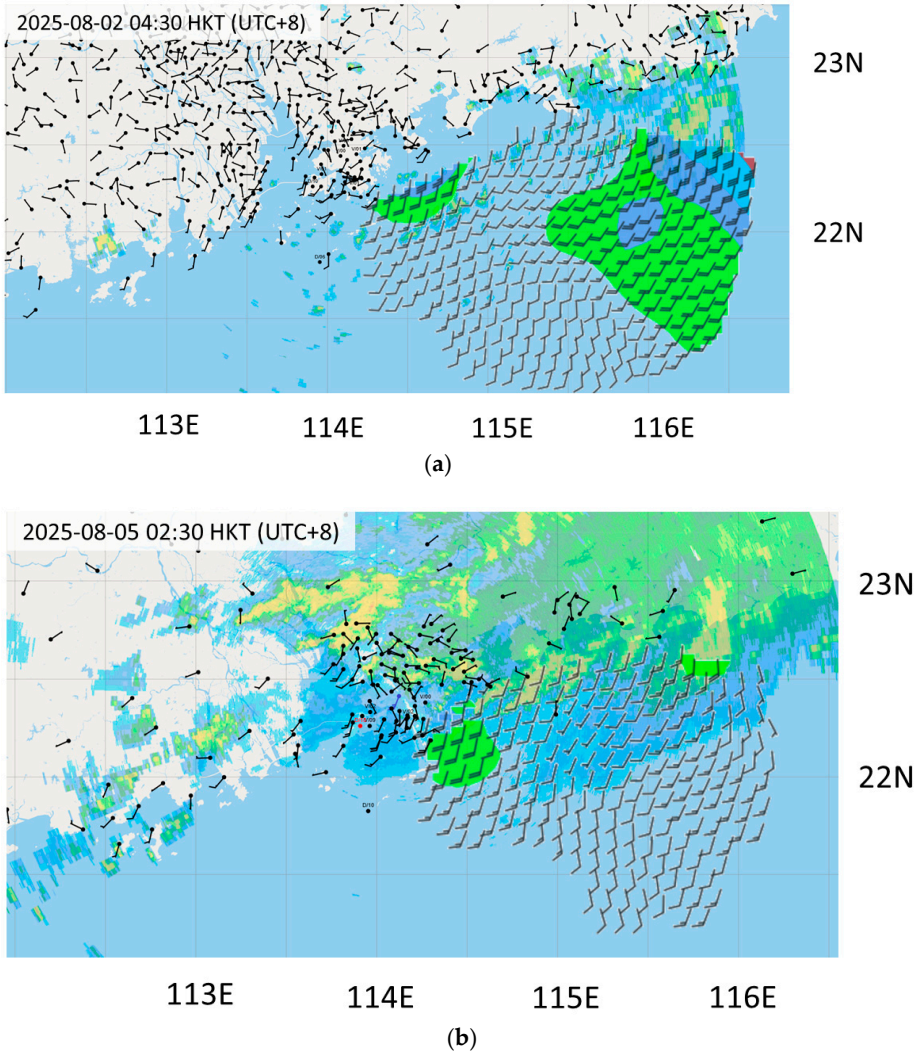

Figure 9. Ocean radar wind output overlaid with weather radar echoes (different colours indicating different rainfall rates, light rain in blue, medium in green and heavy rain in yellow), showing troughing flow in (**a**), and surface observations on land showing surface wind convergence in heavy rain development areas along the coast of eastern China in (**b**) under the prevailing southwest monsoon over the northern part of the South China Sea.

5.4. Tropical Cyclones

Figure 10 is a case of the southwest monsoon prevailing over the South China coast while tropical cyclone Gaemi is affecting eastern China in July 2024. Strong to gale force southwesterly winds are given by the ocean radar at the two time instances as shown in this figure. Though there are no in situ measurements to support winds of such strength, the wind speed and its distribution appear to be reasonable.

It has been reported in a previous study (tropical cyclone Koinu in October 2023) that ocean radar captures well the circulation of the typhoon [26]. A recent case of Typhoon Wipha in July 2025 is shown in Figure 11. Closed circulation is given by the ocean wind directions, consistent with other observations such as weather radar imagery. However, the winds are light compared with the in situ surface observations, e.g., at the island stations and from the weather buoys. The winds are much stronger in this case, reaching gale force, storm force and even hurricane force from the ground stations. The high wind speed may lead to severe folding in the velocity measurement from the ocean radar. Velocity folding seems to begin at a wind speed threshold of around 18 m/s, judging from the comparison plots of ocean radar wind speed against buoy observations in

Figures 3a and 4a. The circulation of the typhoon adds further difficulties to the wind retrieval. As such, ocean radar may work well in more "moderate" winds, such as strong/gale force, even with circulation (as shown in the case of Koinu), but it still has difficulties in situations with too high wind speeds (up to hurricane) and circulating flow at the same time. This would be a topic for further research.

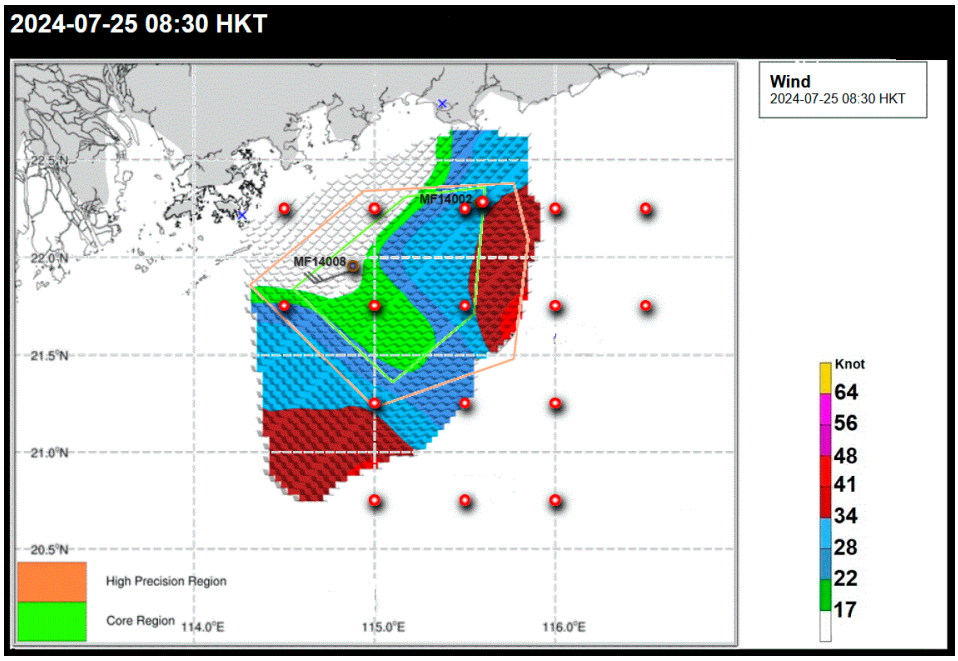

(**a**)

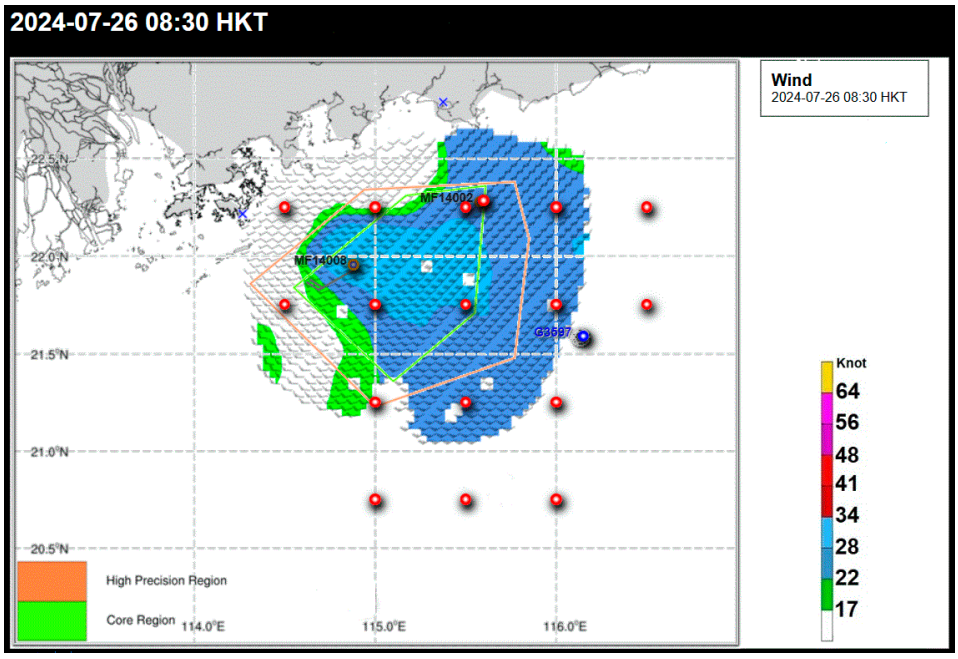

(**b**)

Figure 10. Ocean radar wind output showing (**a**) some gale force southwesterlies over the northern part of the South China Sea brought about by a tropical cyclone over eastern China, and (**b**) southwesterly winds over the seas becoming strong on the next day when the tropical cyclone moved further inland and weakened.

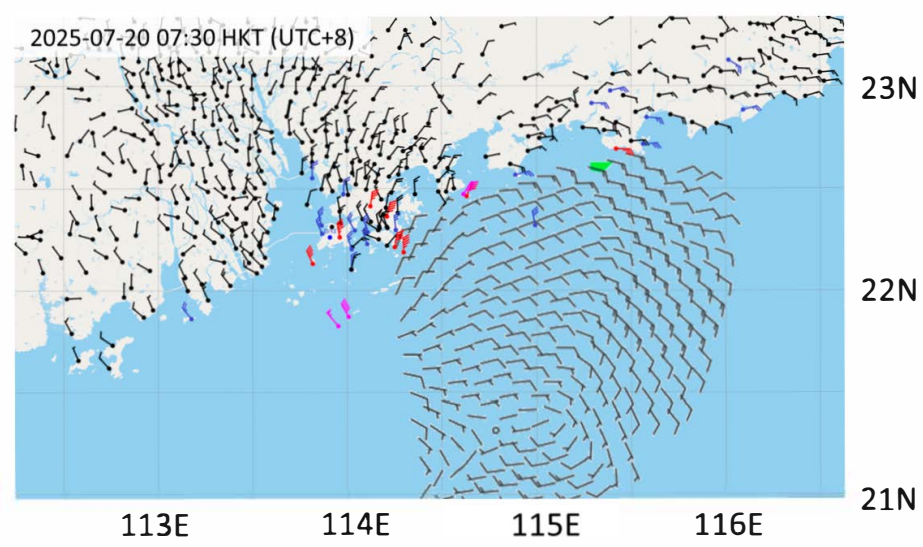

Figure 11. Ocean radar wind output for the circulation of a tropical cyclone.

6. Conclusions

The paper documents the technological advancement with an ocean radar, including both hardware and software, for improving the wind measurements, which are secondary derived products from this equipment.

In terms of software algorithms, the ocean current synthesis process abandons the traditional way of simply relying on geometric relationships and trigonometric functions to restore radial currents to vector currents, and instead adopts the least squares method for restoration. This method can effectively weaken the impact of measurement errors and significantly improve the accuracy of vector current synthesis. Meanwhile, relying on the least squares principle, vector current synthesis breaks through the limitation of the dual-station mode, laying a foundation for subsequent expansion to the multi-station mode. By fusing observation data from multiple stations, it can further expand the spatial coverage of ocean current monitoring and improve data reliability.

In wind and wave inversion, in addition to using the information obtained by the radar itself, fitting adaptation is carried out in combination with buoy-measured data. By comparing and calibrating the radar inversion results with buoy data, the parameters of the inversion model are continuously optimised, making the wind and wave inversion results more reasonable and more in line with the actual marine environment.

At the hardware level, targeted upgrades have been made to the interior of the receiver. The circuit structure of the core processing module has been optimised to reduce noise interference and improve the sensitivity and stability of signal reception. The FPGA programme adopts a more efficient parallel processing architecture, which improves the data processing speed and real-time performance. It can quickly respond to complex ocean echo signals and provide higher-quality raw data support for subsequent algorithm processing.

The ocean radar observations are compared with two sets of weather buoy measurements over an extended period of 1 year, including different weather conditions. In general, the retrieved wind speed and wind direction from the ocean radar are reasonable in terms of correlation coefficients of the scatter data plots and the various error statistics. Further improvements would be required for sea current speed measurements. The wave height from the ocean radar tends to have an underestimation. The application of the ocean-radar-based wind data in a number of meteorological conditions is described. The winds are found to be useful in monitoring monsoon surges, surface trough of low pressure and rainstorms in the southwest monsoon, providing unprecedented details of the winds over the data-void

coastal waters. However, monitoring of the winds of tropical cyclones remains a major challenge to ocean radar, particularly when winds are very strong (reaching hurricane force) and circulating at the same time. This would be an area for further research work.

The software of the ocean radar for the Hong Kong–Shenwei pair would continue to be enhanced in order to obtain the best quality wind data to support weather monitoring, analysis and nowcasting works. A technical roadmap for migrating algorithms validated in the existing literature to the operational system can be pursued. At the signal preprocessing level, we can focus on suppressing ionospheric and radio frequency interference in the range–Doppler spectrum. Higher-order singular value decomposition (HOSVD) has been proven effective in mitigating such interference, which improves the signal-to-noise ratio (SNR) of the echo signal and thus enhances retrieval quality. The next step will then be to engineer this method for practical deployment and to develop robust interference identification capabilities. Furthermore, the wind field detected by radar is a spatial field map rather than isolated single-point data. Within a small domain, the wind field exhibits consistent spatial characteristics, and it also varies gradually (rather than abruptly) in most temporal cases. We can leverage this spatiotemporal continuity to perform quality control (e.g., removing outliers) on the wind field, and further optimise data quality through spatiotemporal assimilation of known data points. However, translating these methods into an operational automatic quality control module and integrating it seamlessly with real-time data streams will require additional time for system development and stability testing.

After further software optimisation, the impact of assimilating ocean radar data into a storm-scale numerical weather prediction model can be explored. All these would be reported in future papers, subject to the performance of the evaluation results.

Author Contributions: Conceptualization, P.-W.C.; methodology, D.H., S.Y. and P.-W.C.; software, D.H. and S.Y.; validation, D.H. and C.-C.L.; formal analysis, D.H., P.-W.C. and S.Y.; investigation, D.H. and C.-C.L.; resources, C.-C.L. and P.-W.C.; data curation, D.H., C.H. and S.Y.; writing—original draft preparation, D.H. and P.-W.C.; writing—review and editing, C.-C.L., C.H. and S.Y.; visualization, D.H. and C.-C.L.; supervision, P.-W.C.; project administration, C.-C.L. and P.-W.C. All authors have read and agreed to the published version of the manuscript.

Funding: This research received no external funding.

Institutional Review Board Statement: Not applicable.

Informed Consent Statement: Not applicable.

Data Availability Statement: The data are available upon reasonable request to the South China Sea Bureau of the Ministry of Natural Resources of China. The data are not publicly available due to privacy.

Acknowledgments: Thanks to the National Marine Data Center, Guangdong-Hong Kong-Macao Greater Bay Area Branch (2024B1212080006) for supporting the provision of buoy and ocean radar data over the South China Sea in this study.

Conflicts of Interest: The authors declare no conflicts of interest.

References

1. Chow, C.K.; Lam, C.C. Journey of Weather Buoys at Seas, the Hong Kong Observatory's Blog. 2022. Available online: https://www.hko.gov.hk/en/Observatorys-Blog/107790/Journey-of-Weather-Buoys-at-Seas (accessed on 26 March 2026).
2. Chen, J.C.; Heinke, G.W.; Zhou, M.J. The Pearl River Estuary Pollution Project (PREPP). *Cont. Shelf Res.* **2004**, *24*, 1739–1744. (In Chinese) [CrossRef]
3. Zhu, H.; Zu, T.; Li, J.; Shu, Y.; Chen, J.; Wang, D. Analysis of tidal current and tidal energy on the west coast of Guangdong Province based on high frequency ground wave radar observation. *J. Trop. Oceanogr.* **2018**, *37*, 25–32. (In Chinese)

4. Barrick, D.E. First-order theory and analysis of MF/HF/VHF scatter from the sea. *IEEE Trans. Antennas Propag.* **1972**, *20*, 2–10. [CrossRef]
5. Schmidt, R.O. Multiple emitter location and signal parameter estimation. *IEEE Trans. Antennas Propag.* **1986**, *34*, 276–280. [CrossRef]
6. Chang, G.; Li, M.; Zhang, L.; Ji, Y.; Xie, J. Measurements of ocean surface currents using shipborne High-Frequency radar. In Proceedings of the IEEE Radar Conference, Cincinnati, OH, USA, 19–23 May 2014; pp. 1067–1070. [CrossRef]
7. Li, C.; Wu, X.; Yue, X.; Zhang, L.; Liu, J.; Li, M.; Zhou, H.; Wan, B. Extraction of Wind Direction Spreading Factor from Broad-Beam High-Frequency Surface Wave Radar Data. *IEEE Trans. Geosci. Remote Sens.* **2017**, *55*, 5123–5133. [CrossRef]
8. Barrick, D.E. Extraction of wave parameters from measured HF radar sea-echo Doppler spectra. *Radio Sci.* **1977**, *12*, 415–424. [CrossRef]
9. Barrick, D.E.; Snider, J.B. The statistics of HF sea-echo Doppler spectra. *IEEE J. Ocean. Eng.* **1977**, *2*, 19–28. [CrossRef]
10. Longuet-Higgins, M.S.; Cartwright, D.E.; Smith, N.D. Observations of the directional spectrum of sea waves using the motions of a floating buoy: Longuet-Higgins, M. S., D. E. Cartwright and N. D. Smith, 1963. In: Ocean Wave Spectra, Proc. Conf., Easton, Md., May 1–4, 1961, Prentice-Hall, N.J., 111–132. *Deep. Sea Res. Oceanogr. Abstr.* **1965**, *12*, 53. [CrossRef]
11. Longuet-Higgins, M.S. The directional spectrum of ocean waves, and processes of wave generation. *Proc. A* **1962**, *265*, 286–315. [CrossRef]
12. Capon, J. High-Resolution Frequency-Wave number Spectrum Analysis. *Proc. IEEE* **1969**, *57*, 1408–1418. [CrossRef]
13. Van Veen, B.D.; Buckley, K.M. Beamforming: A versatile approach to spatial filtering. *IEEE ASSP Mag.* **1988**, *5*, 4–24. [CrossRef] [PubMed]
14. Mitsuyasu, H.; Tasai, F.; Suhara, T.; Mizuno, S.; Ohkusu, M.; Honda, T.; Rikiishi, K. Observation of the directional spectrum of ocean waves using a Clover-Leaf buoy. *J. Phys. Oceanogr.* **1975**, *5*, 750–760. [CrossRef]
15. Davison, A.C.; Hinkley, D.V. *Bootstrap Methods and Their Application*; Cambridge University Press: Cambridge, UK, 1997; 582p.
16. Mokhtar, S.F.; Zahayu, M.Y.; Hasimah, S. Confidence intervals by Bootstrapping approach: A significance review. *Malays. J. Fundam. Appl. Sci.* **2023**, *19*, 30–42. [CrossRef]
17. WMO. Guide to Instruments and Methods of Observation. WMO-No.8 2021/2018 Edition. Available online: https://community.wmo.int/en/activity-areas/imop/wmo-no_8 (accessed on 26 March 2026).
18. Liu, Y.; Li, C.; Yang, Y.; Zheng, B.; Miao, Q.; Xu, S.; Li, W.; Ding, F. Sea surface currents detection in Zhoushan offshore sea by HF surface wave radar. *Mar. Sci. Bull.* **2023**, *42*, 121–127. (In Chinese)
19. Zhang, J.; Dong, X.; Zhu, D. Satellite velocity correction method of ocean current retrieval for a spaceborne Doppler scatterometer. *Remote Sens.* **2023**, *15*, 5541. [CrossRef]
20. Barrick, D.E. Remote sensing of sea state by radar. In Proceedings of the Ocean 72-IEEE International Conference on Engineering in the Ocean Environment, Newport, RI, USA, 13–15 September 1972; pp. 186–192. [CrossRef]
21. Lai, Y.; Wang, Y.; Zhou, H.; Xu, X. Error transfer from radial to total vector current in high-frequency radar oceanic surface current measurement. *J. Huazhong Univ. Sci. Tech. (Nat. Sci. Ed.)* **2021**, *49*, 94–98. (In Chinese) [CrossRef]
22. Wei, G.-M.; Shang, S.-P.; He, Z.-G.; Dong, Q. Performance of wave-wind detection by portable radar HFSWR OSMAR-S100. *Oceanol. ET Limnol. Sin.* **2016**, *47*, 52–60. (In Chinese)
23. Li, C.; Wang, H.; Gao, J.; Li, H.; Wang, G.; Pan, S.; Fan, W.; Liu, K.; Zhao, C.; Qi, A. Data analysis of the high frequency surface wave radar during typhoon Chan-hom. *IOP Conf. Ser. Earth Environ. Sci.* **2017**, *52*, 012019. [CrossRef]
24. Xie, X.; Wu, Y.; Liu, H.; Zhou, W. Data Verification of High Frequency Ground Wave Radar and Its Application in Typhoon Monitoring. *Radar ECM* **2020**, *40*, 43–48. (In Chinese) [CrossRef]
25. Li, L.; Wu, X.; Li, Y.; Long, C.; Liu, B.; Xu, X.A.; Chen, M.; Xue, C. Ocean surface wind and wave monitoring at Typhoon Fung-Wong by HFSWR OSMAR071. *J. Remote Sens.* **2012**, *16*, 154–165.
26. He, J.Y.; Chan, P.W.; Choy, C.W.; Cheung, P.; Chan, Y.W.; Lam, C.C.; He, Y.H.; Rong, P.; Su, H.; Li, Z.M. Multi-Platform Observations of Severe Typhoon Koinu. *Earth Space Sci.* **2024**, *11*, e2023EA003366. [CrossRef]

Disclaimer/Publisher's Note: The statements, opinions and data contained in all publications are solely those of the individual author(s) and contributor(s) and not of MDPI and/or the editor(s). MDPI and/or the editor(s) disclaim responsibility for any injury to people or property resulting from any ideas, methods, instructions or products referred to in the content.